Evolution from Spherical AGB Wind to Multipolar Outflow in Pre-Planetary Nebula IRAS 17150-3224

Po-Sheng Huang[1,2], Chin-Fei Lee[2,1], & Raghvendra Sahai[3]

ABSTRACT

We have mapped the pre-planetary nebula IRAS 17150-3224 in 350 GHz continuum and CO $J = 3$–2 line at an angular resolution of $\sim 0\farcs09$ using the Atacama Large Millimeter/submillimeter Array. A continuum source is detected at the center of the nebula, elongated along the equatorial plane, likely tracing a dusty torus around the central source. Continuum emission is also detected on both sides of the central continuum source in the equatorial plane, probably resulting from interactions of collimated fast winds with envelope material in the equator. CO emission is detected along the optical lobe. Although the optical lobe appears as bipolar, CO map shows that it is actually a quadrupolar outflow consisting of two overlapping bipolar outflows. Two additional younger bipolar outflows are also detected in CO, one at lower latitude and the other along the equatorial plane. In the CO position-velocity maps, blueshifted absorption stripes are detected in the outflow emissions, due to absorption by a series of shells produced by a series of asymptotic giant branch (AGB) wind ejections. By modeling the morphology and kinematics of the AGB wind and outflows, we find that the AGB wind could end $\sim$ 1300 yr ago, the quadrupolar outflow was ejected $\sim$ 350 yr ago, and the two additional bipolar outflows were ejected $\sim$ 280 and 200 ago, respectively. The outflows could be produced either by bullets coming from an explosion, or by a precessing collimated fast wind with a time-dependent ejection velocity.

Subject headings: Asymptotic giant branch stars (2100), Protoplanetary nebulae (1301), Stellar winds (1636), Stellar mass loss (1613), Post-asymptotic giant branch (1287), Stellar jets (1607)

1. Introduction

Pre-planetary nebula (PPN) phase is a short ($\sim$ 1000 yr) evolutionary phase between the asymptotic giant branch (AGB) phase and the planetary nebula (PN) phase for low- to intermediate-mass stars. Most PPNs have developed aspherical morphologies in a few hundred years, possessing toroidal envelope and collimated outflows (Sahai & Trauger 1998; Bujarrabal et al. 2001; Sahai et al. 2007). As a result, PPNs are considered to be the key to answering how spherical AGB winds transform to aspherical PNs (see, e.g., Balick & Frank 2002). Recent observations have shown that bipolar PPNs, e.g., the red rectangle and IRAS 08544-4431 (Bujarrabal et al. 2016, 2018), could be shaped by a disk wind launched from a rotating disk. On the other hand, multipolar PPNs, e.g., CRL 618, could be shaped either by bullets (Balick et al. 2013; Lee et al. 2013a; Huang et al. 2016) or by a precessing collimated fast wind and jet with time-dependent ejection velocity (Riera et al. 2014; Velázquez et al. 2014). The bullets could come from explosive events, producing multipolar outflows. The outflows should have the same age, if the bullets are produced simultaneously. On the other hand, the precessing collimated fast wind and jet could come from a precessing disk, producing multipolar outflows at different angles at different ages.

[1]Institute of Astrophysics, National Taiwan University, Taipei 106, Taiwan ; posheng@asiaa.sinica.edu.tw

[2]Institute of Astronomy and Astrophysics, Academia Sinica, P.O. Box 23-141, Taipei 106, Taiwan

[3]Jet Propulsion Laboratory, MS 183-900, California Institute of Technology, Pasadena, CA 91109, USA

Here we present the Atacama Large Millimeter/submillimeter Array (ALMA) observations of the PPN Cotton Candy Nebula (IRAS 17150-3224; hereafter I17150) at high angular resolution in 350 GHz continuum and CO $J = 3$–2 line. In optical, I17150 appears as a bipolar PPN based on its optical image obtained by the *Hubble Space Telescope* (*HST*)(Kwok et al. 1998). It has a pair of highly extended optical lobes, crossed by many arc structures. It was also observed in CO $J = 1$–0 line (Zuckerman & Dyck 1986; Hu et al. 1993) and $J = 2$–1 line (Hu et al. 1993). The central star is an OH/IR star with a luminosity $L = 27200$ $L_\odot$ and an effective temperature $T_{\rm eff} = 5200$ K (Meixner et al. 2002). Hu et al. (1993) derived a systemic velocity $V_{\rm sys} = 14$ km s^{-1} from the OH maser and the CO $J = 2$–1 observations. The distance to I17150 is not well constrained. Davis et al. (2005) assumed a distance of 2.42 kpc. Meixner et al. (2002) assumed a distance of 3.6 kpc by fitting the galactic HI velocity curve with a systemic velocity $V_{\rm sys}$ of 15 km s^{-1}. In this paper, we assume $d = 3$ kpc as an average and $V_{\rm sys} = 14$ km s^{-1}. We describe our ALMA observations of I17150 in sections 2 and 3; Our model is described in section 4; Discussions are in section 5; Summary of this work is in section 6.

2. Observations

Observations of I17150 were carried out with ALMA in band 7 with 47 antennas in configuration of C40-6 on 2017 August 27. The shortest baseline was ~ 38 m, and the longest baseline was ~ 3.55 km. The target was observed for ~ 50 min. The quasars J1924-2914, J1733-1304, and J1717-3342 were observed for the bandpass, flux, and phase calibration, respectively. The channel width is ~ 244 kHz, giving a velocity resolution of ~ 0.212 km s^{-1} per channel. The calibration and imaging were done by the ALMA pipeline in version r39732.

For the 350 GHz continuum map, a weighting with a robustness parameter of 0.5 was used for the uv visibilities. The synthesized beam has a size of $\sim 0\farcs09 \times 0\farcs06$ with a position angle (P.A.) of $\sim -81°$. The noise level is ~ 0.1 mJy beam^{-1}.

For the CO $J = 3$–2 maps, a weighting with a robustness parameter of 0.5 was adopted for the uv visibilities. The synthesized beam has a size of $\sim 0\farcs09 \times 0\farcs06$ with a P.A. of $\sim -76°$. The noise level in the representative spectral window of CO is ~ 1.7 mJy beam^{-1} for a channel width of 0.212 km s^{-1}.

3. Results

3.1. 350 GHz Continuum

Figure 1 shows the continuum map of I17150 at 350 GHz, superimposed on the optical image taken by the *HST* with filter F606W (Kwok et al. 1998). Three continuum components are detected in continuum, with one at the center, one in the east (ECC), and one in the west (WCC) in the equatorial plane. They have a total extent of $\sim 2\farcs6$ (~ 7800 au) along the equator. The central component is elongated along the equatorial plane with a primary peak at the center of the nebula (Figure 1b) and thus likely traces a torus around the central source of I17150, as included in the circumstellar envelope model proposed in Meixner et al. (2002). The ICRS coordinate of the primary peak is R.A. = $17^{\rm h}18^{\rm m}19\fs875$, Dec. = $-32°\ 27'\ 21\farcs8$. A secondary peak is seen at a distance of ~ 550 au ($0\farcs18$) to the southwest of the primary peak and seems to be spatially aligned with the linear optical emission there in the dust lane. The eastern and western components are located at a large distance of $\sim 1''$ (~ 3000 au) from the central component, and thus could trace materials produced and dragged away by winds or jets from the central source, as discussed later.

The total flux density of the continuum in the three components is ~ 0.3 Jy, amounted to $\simeq 40\%$ of the value (~ 0.8 Jy) previously reported at a similar frequency in Hu et al. (1993) with James Clerk Maxwell Telescope (JCMT) at a resolution of $\sim 19''$. This suggests that although the three components here are compact, they have a flux density comparable to that of the extended component (AGB wind). Assuming that the continuum emission is all thermal dust emission and optically thin, the dust mass producing the continuum emission can be roughly estimated from the following equation:

$$M_d \simeq \frac{D^2 F_\nu}{B_\nu\left(T_d\right)\kappa_\nu}, \qquad (1)$$

where D is the distance to I17150, F_ν is the flux density, $B_\nu\left(T_d\right)$ is the Plank blackbody function

at the dust temperature $T_d \sim 150$ K (Meixner et al. 2002; de Vries et al. 2015), and κ_ν is the dust grain opacity. Assuming that the dust grains are similar to to those around evolved stars (Dharmawardena et al. 2018), we have $\kappa_\nu = 0.3$ cm^2 g^{-1} at 350 GHz, and thus $M_d \sim 7\times10^{-2}$ M$_\odot$.

The gas-to-dust mass ratio of the circumstellar envelope of I17150 is unknown. Previously, Meixner et al. (2002) adopted a ratio of 280 as in the shell of the OH/IR star OH 26.5+0.6 (Justtanont et al. 1996). Using this ratio, we derive a shell mass of ~ 20 M$_\odot$, which seems too big for an OH/IR star, like our source. Thus, we adopt a ratio of 77, as found in the circumstellar envelope around O-rich stars (Dharmawardena et al. 2018) to calculate the mass and find it to be $\sim$ 5.4 M$_\odot$, which is more reasonable for an OH/IR star.

3.2. CO Intensity and Velocity Maps

Figure 2a shows the total intensity map (red image) of the CO J = 3–2 emission integrated from -15 to 45 km s^{-1}, superimposed on the *HST* image (turquoise image). It shows a quadrupolar outflow consisting of two overlapping bipolar outflows, Q1 and Q2, along the optical lobes. It also shows two additional bipolar outflows, B1 at a lower latitude and B2 along the equator, that have not been detected before.

Figure 2b shows the intensity-weighted (radial) velocity map toward the nebula, in order to identify different velocity components of the outflows. The solid lines indicate the axes of the quadrupolar outflow Q1 and Q2, and the bipolar outflows B1 and B2. As can be seen, outflow Q1 has a blueshifted lobe (Q1b) in the northwest and a redshifted lobe (Q1r) in the southeast, whereas outflow Q2 has a blueshifted lobe (Q2b) in the southeast, and a redshifted lobe (Q2r) in the northwest. Thus, Q1 and Q2 have opposite inclination angles to the plane of the sky. The length and width of the lobes in Q1 and Q2 are $\sim$ 3.″2 (9600 au) and 1″ (3000 au), respectively. At a lower latitude, outflow B1 has a redshifted lobe (B1r) in the west. In the east, the blueshifted lobe (B1b) roughly along the Q2b axis is considered here to be the blueshifted counterpart, although it appears deflected from the B1 axis by $\sim 17^\circ$ counterclockwise. The length of lobe B1b is $\sim$ 1″ (3000 au), about half of lobe B1r, which is $\sim$ 2″ (6000 au). Outflow B2 has a blueshifted lobe (B2b) in the southwest, and a redshifted lobe (Q2r) in the northeast along the equator, aligned with the major axis of the continuum emissions. The length and width of lobes B2b and B2r are $\sim$ 1.″4 (4200 au) and 0.″8 (2400 au), respectively. Most of the outflows are reasonably symmetric, except for outflow B1.

3.3. CO Line Profile

Figure 3 shows the CO J = 3–2 line profile averaged over an elliptical region with a major axis of 7″, a minor axis of 4″, and P.A. = -56°, covering all the outflows. The emission is detected from -15 to 45 km s^{-1}. The line profile has a peak flux of $\sim$ 8.6 Jy at $\sim$ 16 km s^{-1}, which is $\sim$ 2 km s^{-1} redshifted from the systemic velocity. It appears asymmetric about the systemic velocity, mainly due to an absorption dip from ~ -1 to 12 km s^{-1} produced by the front part of a cooler AGB wind, as discussed in Section 3.5.

3.4. CO Channel Maps

The detailed velocity distribution of the outflow lobes can be studied with the CO J = 3–2 channel maps shown in Figure 4. In order to increase the signal-to-noise ratio to better see the velocity distribution, we binned 15 channels to one single wide channel with a velocity width of $\sim$ 3.2 km s^{-1}. The outflow lobes can be better distinguished at high velocities. For example, four blueshifted outflow lobes Q1b, Q2b, B1b, and B2b are clearly seen in high blueshifted-velocity channels at -11.4, -8.26, and -5.08 km s^{-1}, and four redshifted outflow lobes Q1r, Q2r, B1r, and B2r are clearly seen in high redshifted-velocity channels at 33.1 and 36.2 km s^{-1}. At low velocity around the systemic velocity (14.0 km s^{-1}), the CO emission traces the limb-brightened cavity walls of the outflows. Interestingly, the cavity walls of the 4 lobes (Q1b, Q1r, Q2b, and Q2r) in the quadrupolar outflow merge side by side, appearing as a bipolar outflow around the optical bipolar lobe. This is probably because the outflow lobes interact with each other, and the CO molecules in the interacting zones have been dissociated by the interaction.

From the systemic-velocity channel (at 14.0 km s^{-1}) to the high-velocity channels (to -11.4

km s^{-1} on the blueshifted side and to 36.2 km s^{-1} on the redshifted side), the CO emission of the quadrupolar outflow shows lobe structures that narrow down to the outflow axis and shrink towards the outflow tips. Since the lobe structure in each channel map comes from a sectional view of the outflow lobes, this indicates that the outflow lobes are hollow and ellipsoidal and has a velocity increasing towards the tips. At the systemic-velocity channel, the outflow shells can be seen clearly and have a thickness of ∼300 au. In the velocity range from 1.27 km s^{-1} to 7.63 km s^{-1}, the CO emission is weaker than that in the other velocity range, because the emission is mostly absorbed by a front part of the AGB wind, as implied from the absorption dip in the line profile shown in Figure 3.

Outflow B2 is along the equatorial plane, roughly aligning with the axis connecting the eastern (ECC) and western continuum components (WCC), as shown in Figure 5. ECC is inside the redshifted lobe B2r, extending towards its tip. WCC has two parts, with the inner part located right inside the tip of the blueshifted lobe B2b, and the outer part right outside the tip. ECC and WCC could result from interactions between the outflow and AGB wind or torus in the equator.

At low velocity, as in the channels of 7.63–23 km s^{-1} in Figure 4, when we look into the very center within 0.″7 of the central source, we see an additional smaller bipolar structure extending out from the source along the symmetry axis of the optical lobes (P.A. = −64°). Figure 6 shows the zoom-in in the central low-velocity channels of 10.8–17.2 km s^{-1} in order to better study the their structures. The blueshifted (Figure 6a) and redshifted (Figure 6c) emissions show a pair of U-shaped cavity walls, which have a total length of ∼ 1800 au (0.″8) and a width of ∼ 1800 au (0.″6). The cavity walls have a symmetry center at the primary peak of the continuum emission (Figure 6b) and are thus produced by the central source, tracing the walls of an outflow (hereafter outflow B3) near the central source.

3.5. Position-Velocity Diagrams

Position-velocity (PV) diagrams can be used to reveal the kinematics of the outflow lobes. Figure 7a, 7b, 7c, and 7d show the PV diagrams of the CO J = 3–2 emissions cut along the axes of outflows Q1, Q2, B1, and B2, respectively. The position of the central source (0″) and systemic velocity (14 km s^{-1}) are indicated by horizontal and vertical dashed lines, respectively. In Figure 7a, lobes Q1b and Q1r are seen with two big tilted elliptical PV structures, as expected if they are expanding shells driven by collimated fast winds (CFWs) (Lee et al. 2001). Interestingly, on the blueshifted side, a series of slightly bended absorption stripes with a velocity ranging from ∼ 0 to 12 km s^{-1} are detected. They are mainly vertical but bended slightly towards the systemic velocity. As discussed later, they are due to the absorption by a series of dense AGB shells in front of the outflow lobes. Within 1″ of the central source, a smaller bipolar PV structure is seen coming from outflow B3 lying along the axis of outflow Q1.

In Figure 7b, two similar large elliptical PV structures are seen coming from lobes Q2r and Q2b, but with an opposite tilt because of an opposite inclination. Again, the smaller bipolar PV structure comes from outflow B3 that lies along the outflow axis of Q2. In addition, emissions (as marked as Q1b, Q1r, and B1b) are also seen from outflows Q1 and B1 that lie along the outflow axis of Q2.

Figure 7c shows PV structures along the B1 (B1r) axis and the B1b axis (which is deflected by 17° from the B1 axis). The length of lobe B1r is nearly twice the length of lobe B1b. The B1b axis also crosses lobe Q1r in the south, showing some emission from lobe Q1r in the lower part of the PV diagram. The emissions at the center are from outflow B3, similar to those seen in Figure 7a and 7b.

In Figure 7d, the emissions from lobes B2r and B2b form similar elliptical PV structures and collimations to those seen from the quadrupolar outflow lobes, and thus could also be shaped by a CFW. In this diagram, the cut is roughly along the equatorial plane crossing the base of outflow B3. The emission there forms a single elliptical lobe structure, indicating that the base of outflow B3 is expanding equatorially.

3.5.1. Expansion Velocity of the AGB Wind

The absorption stripes can be linked to the arc structures in the optical image, which are due to a

periodically enhanced mass loss of the AGB wind (Kwok et al. 1998), allowing us to estimate the expansion velocity of the AGB wind. Previously, seven arc structures, A, B, C, D, E, F, and G, have been identified at a distance of $\sim 1\farcs2$, $1\farcs7$, $2\farcs2$, $2\farcs7$, $3\farcs2$, $3\farcs9$, and $4\farcs6$, respectively, as shown in Figure 8b, tracing a series of dense spherical expanding shells. Their emission is expected to produce a series of elliptical PV curves centered at the systemic velocity in the PV diagram. However, since they are cooler than the outflows, the outflow emissions are absorbed by the front part of the AGB shells in front of the outflows, producing the absorption stripes only on the blueshifted side, as seen in the PV diagram.

The expansion velocity can be determined from the semi-major axis of the (half) elliptical PV structure. Unfortunately, the semi-major axis of the absorption stripes can not be clearly identified from the observed PV diagram. Since the separation between two consecutive arcs is roughly the same for the inner arcs but increases from arc D to arc E (see Figure 8b), we assume the expansion velocity to be the same for the inner arcs and to increase from arc D to arc E. From modeling the absorption stripes with this assumption, the expansion velocity of inner arcs A, B, C, and D are found to be ~ 13 km s^{-1}, and the expansion velocity of the outer arcs E, F, G, and etc are found to be ~ 14.4 km s^{-1}, with a small velocity jump from arc D to arc E, as shown in Figure 9. As can be seen, the resulting model absorption stripes (as indicated by the dashed curves) can match the observed absorption stripes reasonably well (Figure 8a). Further observations at higher sensitivity are needed to derive a precise value of the velocity jump from the PV diagrams.

The dynamical ages of arcs A, B, C, D, E, F, G, and H are estimated to be ~ 1300, 1850, 2410, 2970, 3180, 3860, 4550, and 5230 yr, respectively (see Figure 9), using the distance and expansion velocity of the arcs in our model. Thus, the time durations of the inner and outer arcs are ~ 550 and 680 yr, respectively. Hence, the AGB wind velocity appeared to decrease slightly from 14.4 to 13 km s^{-1} at ~ 3200 yr ago.

4. Model for I17150

Here we derive the physical properties (including temperature, density, velocity, and the mass-loss rate) of the AGB wind and the outflows by modeling their observed intensity maps, line profile, and PV structures in CO $J = 3$–2. The aim is to determine the mass-loss process in the end of the AGB phase and the shaping mechanism of the outflows. Our model consists of a spherical AGB wind, a quadrupolar outflow, and three pairs of bipolar outflows, as shown in Figure 10. The physical properties of the AGB wind and outflows in our model are described as follows.

4.1. AGB Wind

Based on the optical arcs observed in the *HST* image, the AGB wind is assumed to be spherical with a periodical density enhancement. Thus, the density of the AGB wind can be written in spherical coordinates as

$$\rho_{\rm a}(r) = \frac{\dot{M}_{\rm a}(r)}{4\pi r^2\, v_{\rm a}(r)}, \qquad (2)$$

where r is the radial distance to the center, and $\dot{M}_{\rm a}(r)$ is a r-dependent mass-loss rate to account for the periodical density enhancement. The variation amplitude in mass-loss rate is unknown. Here we use the following simple form for the first attempt,

$$\dot{M}_{\rm a}(r) = \begin{cases} 2\cos^2(\pi\,(r - r_{\rm A})\,/\Delta r_1)\dot{M}_{\rm a,0}, & \text{if } r \le r_{\rm E} \\ 2\cos^2(\pi\,(r - r_{\rm E})\,/\Delta r_2)\dot{M}_{\rm a,0}, & \text{if } r > r_{\rm E} \end{cases}, \qquad (3)$$

where the averaged AGB mass-loss rate $\dot{M}_{\rm a,0} = 5.3 \times 10^{-4}$ M$_\odot$ yr^{-1}, as in the model of Meixner et al. (2002). As estimated from the *HST* image, $r_{\rm A}$ and $r_{\rm E} = 3555$ and 9675 au, respectively. The arc separations Δr_1 for the inner arcs and Δr_2 for the outer arcs are ~ 1530 au ($0\farcs51$) and 2070 au ($0\farcs69$), respectively. The density crests are located at the radii of the arcs, where $r = r_{\rm A}$, $r_{\rm A} + \Delta r_1$, ..., $r_{\rm E}$, $r_{\rm E} + \Delta r_2$, ..., etc.

The expansion velocity of the AGB wind has been estimated earlier by modeling the absorption stripes in the PV diagram. It can be written with the following form

$$v_{\rm a}(r) = \begin{cases} 13 \quad {\rm km\,s^{-1}}, & \text{if } r \le r_{\rm D} \\ 13 + 1.4\frac{r-r_{\rm D}}{r_{\rm E}-r_{\rm D}} \quad {\rm km\,s^{-1}}, & \text{if } r_{\rm D} < r < r_{\rm E} \\ 14.4 \quad {\rm km\,s^{-1}}, & \text{if } r \ge r_{\rm E} \end{cases}, \tag{4}$$

For the AGB wind temperature, we assume a power-law distribution with

$$T_{\rm a}(r) = T_{\rm a,0} \left(\frac{r}{r_{\rm A}}\right)^{\gamma_{\rm a}}, \tag{5}$$

where $T_{\rm a,0}$ is the temperature at the radius of arc A, and $\gamma_{\rm a}$ is the temperature power-law index for the AGB wind.

4.2. Outflows

For simplicity, the outflow lobes can be assumed to be ellipsoidal for Q1, Q2, B1r and B2, and U-shaped (with a bottom half of an ellipsoid) for B1b and B3, as shown in Figure 11. Note that lobe B1b is assumed to be a bottom half of an ellipsoid because it shows a wide opening angle at the top and has a length only half that of lobe B1r (Figure 2b). Table 2 lists the lengths l_f and widths D_f (f is either Q1, Q2, B1, B2, or B3) of the outflow lobes measured from the intensity-weighted velocity map in Figure 2b.

The thickness of the outflow shells (or cavity walls) can not be accurately determined from the observations, because it could be smaller than the beam size of $0\farcs09 \times 0\farcs06$. Following the simulation results in, e.g., Lee & Sahai (2003), the outflow shells here are assumed to be thicker at higher latitude and thinner at lower latitude. To construct such shells, each shell is assumed to be bounded by an outer ellipsoid and an inner ellipsoid, as shown in Figure 11. In addition, the lengths and widths of the inner ellipsoids are assumed to be smaller than the outer ellipsoids by 600 au. Then with the center of the inner ellipsoid shifted by 300 au towards the central source, the shells have a thickness increasing from 0 au at the base to 600 au at the outflow tips. In addition, since the bottom of outflow B3 showed an expanding ring-like structure in the PV diagram (Figure 7d), outflow B3 is assumed to be two slightly merged bottom-half ellipsoids with a non-zero width at the base.

Assuming that the outflows mostly consist of shocked or swept-up AGB wind (Lee & Sahai 2003), their density is expected to be proportional to r^{-2}, as in the AGB wind. Thus the density of the outflow shells can be expressed by

$$\rho_f(r) = 1.4\, m_{\rm H_2}\, n_{f,0} \left(\frac{r}{l_f}\right)^{-2}, \tag{6}$$

where $m_{\rm H_2}$ is the mass of a molecular hydrogen, $n_{f,0}$ is the number density of molecular hydrogen at the tips of the outflows. Helium is also included, with its number density $n_{\rm He} = 0.1 n_{\rm H}$.

The outflow emissions are mostly produced by the shocked AGB wind, and the strongest shocks are at the outflow tips. Therefore, the highest temperature is expected to be found at the outflow tips. Furthermore, since we assume that the density varies as r^{-2}, the temperature needs to increase with r, in order to reproduce the observed ratio (roughly unity) of the emission intensity at the outflow tips relative to that at the outflow bases. Thus, we assume that

$$T_f(r) = (T_{f,0} - 20\,K) \left(\frac{r}{l_f}\right)^{\gamma_f} + 20 \ {\rm K} \tag{7}$$

where $T_{f,0}$ is the temperature at the tips of the outflows, and γ_f is the temperature power-law index.

As for the outflow velocity structures, we assume that the velocity decreases from the tips to the bases using the following form for outflows Q1, Q2, B1, and B2:

$$\boldsymbol{v}_f = v_{f,0} \exp\left[-\left(\frac{\theta}{\theta_f}\right)^{\beta_f}\right] \hat{\boldsymbol{r}}, \tag{8}$$

where θ is the angle of the position vector $\boldsymbol{r}$ measured from the axes of outflows, $v_{f,0}$ is the velocity at the outflow tips (where $\theta = 0°$), θ_f is the opening angle, and β_f is a power-law index for the decrease of the velocity. Our velocity form is similar to the input velocity of the wind in Lee & Sahai (2003). In general, the outflow velocity decreases from the pole to the equator as seen in the simulations, but may decrease slower than the actual outflow velocity in the simulations. We also do not include the converging flow seen in the simulations of the bipolar outflow models (e.g., Lee & Sahai 2003; Balick et al. 2019), because the emission detected here are mostly shocked AGB

wind instead of shock wind material.

Unlike other outflows, outflow B3 has a non-zero expansion velocity at the base, as implied from the PV diagram (Figure 7d). In addition, the velocity of outflow B3 can decrease differently in z and R directions. Thus, we assume separate equations for the two directions:

$$\boldsymbol{v}_z = v_{\rm B3z,0} \left(\frac{90^\circ - \theta}{90^\circ - \theta_{\rm B3}} \right) \hat{\boldsymbol{z}}, \quad (9)$$

$$\boldsymbol{v}_R = v_{\rm B3R,0} + (v_{\rm B3R,1} - v_{\rm B3R,0}) \left(\frac{\theta - \theta_{\rm B3}}{90^\circ - \theta_{\rm B3}} \right) \hat{\boldsymbol{R}}, \quad (10)$$

where $\sqrt{v_{\rm B3z,0}^2 + v_{\rm B3R,0}^2} = v_{\rm B3}$ is the velocity at the tops of outflow B3 [where $\theta = \theta_{\rm B3} = \arctan(0.5 D_{\rm B3}/l_{\rm B3})$], and $v_{\rm B3R,1}$ is the velocity at the base.

4.3. Model Results

Tables 1 and 2 list the best-fit parameters in our model. The CO $J = 3$–2 emissions are calculated using a radiative transfer code with an assumption of local thermal equilibrium (Huang et al. 2016). In addition, we assume a CO abundance of 2×10^{-4}, similar to that of the circumstellar envelopes of O-rich stars (Woods et al. 2005).

The following criteria are used to judge the goodness of our model: (1) In the CO $J = 3$–2 line profile, the model flux intensity peaks (one on the blueshifted side, one near the systemic velocity, and one on the redshifted side) and the absorption dip (between -1 to 12 km s^{-1}) should be consistent with the observed values within 15%, as shown in Figure 12. (2) In channel maps (Figure 13), the model morphology (including the outflow lengths, widths, position angles, etc.) and the flux intensity should be consistent with those measured from the observed channel maps (Figure 4). A minor difference can come from the high-velocity emissions at the outflow tips (e.g., in the first and last channels of the channel maps), because we assume outflows Q1, Q2, and B2 (except outflow B1) are symmetric in our model, but the observed outflow velocity is slightly asymmetric. (3) The model PV structures along the outflow axes Q1, Q2, and B2 should appear as tilted ellipses (Figure 14), as in the observed PV diagrams (Figure 7). Moreover, the curvatures and velocity ranges of the model PV structures and the velocity at outflow tips should be consistent with the observations. (4) The outflow shells should be partially absorbed by the front part of the AGB wind, producing broken PV structures as in the observed PV diagrams. The periodic density enhancement of the AGB wind should produce the absorption stripes in the PV diagrams (Figure 14), with the outflow emissions fully absorbed by AGB material in the arcs and partially absorbed by AGB material in between arcs. The AGB wind mass-loss rate of 5.3×10^{-4} M$_\odot$ yr^{-1} appears to be reasonable because the model spectrum can fit the observed one as shown in Figure 12.

Note that unlike the observed PV diagrams (Figure 7), we do not see any faint emission inside the elliptical PV structures (Figure 14), likely because we do not include any tenuous gas inside the outflow lobes in our model.

In our model, the velocities at the tips of outflows Q1, Q2, B1, B2, and B3 are $\sim$ 130, 130, 100, 100, and 80 km s^{-1}, respectively. The resulting dynamical ages are $\sim$ 350 yr for outflows Q1 and Q2, 280 yr for outflow B1, 200 yr for outflow B2, and 50 yr for outflow B3. The total mass of the outflows are $\sim$ 0.6 M$_\odot$.

5. Discussions

5.1. New Features of I17150

We have identified four new features in I17150. Firstly, although this object shows a bipolar morphology in the optical, it shows a quadrupolar outflow in CO, with two overlapping bipolar outflows. These two bipolar outflows partially merge, appearing as a single bipolar outflow as seen in the optical. These two bipolar outflows have opposite inclinations to the plane of the sky, as found in the velocity map. They both have a dynamical age of $\sim$ 350 yr.

Secondly, the quadrupolar outflow is followed by two more younger bipolar outflows ejected along two different directions. One is along the B1 axis in between the symmetry axis of the quadrupolar outflow and the equatorial plane, with a dynamical age of $\sim$ 280 yr. Another one is almost on the equatorial plane and has a dynamical age of $\sim$ 200 yr.

Thirdly, a bipolar outflow, B3, is seen near the central source, appearing as a U-shaped cavity wall on each side of the source. It may consist of shocked toroidal envelope resulting from an interaction between the torus and an underlying wind, jet, or bullet coming from the central source, as seen in Huang et al. (2016).

Fourthly, a series of absorption stripes are detected in the CO PV diagrams, associated with the optical arcs. These arcs trace a series of spherical expanding shells produced by a periodically enhanced mass loss of the AGB wind. These shells are cooler than the outflows and thus absorb the CO emission of the outflows, producing the observed absorption stripes in the PV diagrams. By modeling the absorption stripes, we find that the expansion velocity of the AGB wind is $\sim$ 13.0 km s^{-1} for inner shells and 14.4 km s^{-1} for the outer shells, and decreases slightly from 14.4 to 13.0 km s^{-1} from the outer to inner shells 3200-3000 yr ago. The underlying reason for this velocity decrease is unclear. It may due to a decrease in escape velocity around the central source, which in turn can be due to a decrease in stellar mass and/or the luminosity (Górny et al. 1994).

5.2. When did the AGB Phase End?

In the optical image, arc A is the innermost arc detected in the flux intensity profile along the southern lobe. There could be more arcs within arc A, but their intensity could be too weak to be distinguished from that of the optical lobes in the intensity profile. In our observations, we also could not determine if there are more arcs within arc A, because those arcs, even if present, could not fully absorb the strong CO outflow emission there to produce clear absorption stripes.

In our model, arc A was ejected at $\sim$ 1300 yr ago. If there is no more arc ejected after arc A, then the time delay between the end of the AGB wind and the start of the outflow would be $\sim$ 1300 $-$ 350 = 950 yr, which seems too long comparing to the previously estimated time delay (with a median of 300 yr) between the jets and tori (Huggins et al. 2007). However, if there was indeed one more arc ejected after arc A, that arc would be ejected $\sim$ 750 yr ago, assuming the same ejection period of 550 yr as the other inner arcs. In that case, the time delay would be $\sim$ 750 $-$ 350 = 400 yr, well consistent with the previously estimated time delay. On the other hand, if the AGB wind continued until the ejection of the quadrupolar outflow, there would be no time delay between the end of the AGB wind and the start of the outflow, so the source of the AGB wind and the sources of the outflows would be different. For example, the AGB wind and the outflows could be ejected from the primary star and the companion, respectively, in a binary system. More observations are needed to check which scenario is correct.

5.3. Possible Shaping Mechanisms for the Quadrupolar Outflow

The quadrupolar outflow consists of two bipolar outflows Q1 and Q2 with the same size and dynamical age, suggesting that they are produced simultaneously. Many scenarios have been proposed to produce bipolar outflows (Huggins et al. 2007): a magnetic wind from a single star or a binary; an accretion disk around a binary companion or a primary. If the quadrupolar outflow was shaped by two bipolar winds, each bipolar wind should be ejected from one star. However, the chance of simultaneously producing two bipolar winds from two stars is very low. On the other hand, like the multipolar outflows seen in other objects, e.g., in CRL 618 (Sahai 2004; Lee et al. 2013a), the quadrupolar outflow could be shaped either by a precessing collimated fast wind with time-dependent ejection velocity (Montgomery 2012; Velázquez et al. 2012, 2013; Riera et al. 2014) or by multidirectional bullets (Matt et al. 2006; Balick et al. 2013; Huang et al. 2016). If the two bipolar outflows were shaped by a precessing collimated fast wind, they should have different dynamical ages. Thus, the quadrupolar outflow seems to be shaped by multidirectional bullets.

Multidirectional bullets could come from an explosive event, e.g., a magneto-rotational explosion or a nova-like explosion (Matt et al. 2006; Balick et al. 2013; Lee et al. 2013b; Huang et al. 2016). In the case of the magneto-rotational explosion, the central star spins so fast that the magnetic field above the surface of the star is highly twisted. Thus, the magnetic pressure force could drive the magneto-rotational explosion, ejecting bullets (clumps of mass) in many directions. In the 2nd case, a nova-like explosion is triggered by the

accretion of gas from a primary onto a white dwarf companion. The hydrogen gas can be pulled onto the surface of the white dwarf and then form an envelope massive enough to ignite a hot CNO cycle in a nova explosion (Wiescher et al. 2010).

In our observations, the central region could indeed harbor a binary system, with the continuum map showing a primary peak at the center of the quadrupolar outflow and a secondary peak in the west along the equatorial plane. It is possible that the star at the secondary peak is losing a part of its mass to the star at the primary peak, forming an accretion disk and torus around the star there.

In previous study, IRAS 19475+3119 was also found to be a quadrupolar PPN proposed to be shaped by two intrinsically collimated winds or jets (Hsu & Lee 2011), but the launching mechanism for the winds or jets is still unclear. If the quadrupolar outflow lobes of IRAS 19475+3119 have the same dynamical age, they could also be produced by multidirectional bullets.

5.4. A Precessing Collimated Fast Wind Model for the Younger Outflows

In addition to the quadrupolar outflow, we have also detected two younger bipolar outflows B1 and B2 at lower latitudes, with B2 along the equatorial plane and B1 in between the polar axis and equatorial plane. Similar low latitude outflows or equatorial outflows have been observed in other PPNs, such as Egg Nebula (Sahai et al. 1998; Cox et al. 2000; Balick et al. 2012), Frosty Leo Nebula (Sahai et al. 2000), and CRL 618 (Cox et al. 2003; Lee et al. 2013a).

According to our model, the two low-latitude outflows were ejected 280 and 200 yr ago, respectively, both younger than the quadrupolar outflow (350 yr). Since these two outflows are younger than the quadrupolar outflow, it is not clear if they can be produced by the same explosive bullets as for the quadrupolar outflow. Unlike the quadrupolar outflow lobes produced by bullets with the same dynamical age, the two low-latitude outflows with different dynamical ages could be produced by different mechanism. Interestingly, for these outflows, their dynamical ages decrease with their latitudes: Q1 = Q2 > B1 > B2, probably suggesting that the outflow axes have changed from high latitude to lower latitude in $\sim$ 150 yr. But there is insufficient data to determine the dynamical ages for other objects with multipolar outflows at low latitude.

A rapid change of the outflow direction has been proposed in the precessing jet model for PPN CRL 618 (Riera et al. 2014) and the binary model for bullet ejections of the carbon star V Hydrae (Sahai et al. 2016). In these two models, the jet and bullets are ejected near the periastron passage of a binary companion orbiting in a highly eccentric orbit (Soker & Mcley 2013). In addition, a precessing jet with a time-dependent ejection velocity could produce non-overlapping lobes (Riera et al. 2014). If the outflow source of I17150 is also a binary, the orbital period and velocity variation period can be obtained from the time durations between the outflows, which are $\sim$ 70–80 yr. The precessing period of the disk would be two times the time duration between the quadrupolar outflow and the equatorial outflow (assuming that they were produced at opposite directions). The precessing period is thus $\sim$ 300 yr, which is four times the orbital period as in the precessing jet model of Riera et al. (2014).

One possibility of the outflow formation mechanism is shown in Figure 15. At the beginning, the explosion, either magneto-rotation explosion or nova-like explosion, produced the bullets creating the quadrupolar outflows Q1 and Q2. Then, the disk precessed by $\sim 35^\circ$ to produce the B1 lobes, and then precessed more by $\sim 30^\circ$ to produce the B2 lobes. Producing this large precessing of the disk would require a binary companion with an orbital plane significantly misaligned with the disk plane (Terquem 1998).

6. Summary

We have mapped the AGB wind and outflows in I17150 with ALMA at $\sim 0\farcs09$ resolution. A continuum source is detected with a primary peak at the center of the outflows. It is elongated along the equator, likely tracing a dusty torus around the central source. It also has a secondary peak at $\sim$ 550 au to the east along the equatorial plane, and further observation is needed to study its origin. Two additional continuum emissions are also detected on either side of the central continuum source, probably resulting from interactions of CFWs with the envelope along the equator.

Along the optical lobes, two overlapping bipolar outflows are detected in CO, forming a quadrupolar outflow. They have roughly the same dynamical age of $\sim$ 350 yr. They could be produced by bullets from an explosion such as a magneto-rotational explosion or a nova-like explosion. Two younger bipolar outflows are detected with one at a lower latitude ejected 280 yr ago and one along the equator ejected 200 yr ago. They could be produced by a precessing CFW with time-dependent ejection velocity. The PV structures of all the outflows appear as tilted ellipses, consistent with a wind-driven shell model. In addition, a pair of U-shaped cavity walls are detected at the center, probably tracing shocked toroidal envelope resulting from an interaction with a bipolar wind.

Absorption stripes are detected in the PV diagrams of the outflow emissions in CO, due to the absorption by cooler AGB shells in front of the outflows. By modeling the absorption stripes, we find that the expansion velocity to be $\sim$ 14.4 km s^{-1} for the outer shells and 13 km s^{-1} for the inner shells. The ejections of the AGB wind could have ended after the ejection of the innermost shell at $\sim$ 1300 yr ago. The time delay between the AGB wind and the outflows is $\sim$ 1000 yr, but it could be shorter if there were additional AGB shell within the detected innermost shell.

This paper makes use of the following ALMA data: ADS/JAO.ALMA#2016.1.01530.S. ALMA is a partnership of ESO (representing its member states), NSF (USA) and NINS (Japan), together with NRC (Canada), MOST and ASIAA (Taiwan), and KASI (Republic of Korea), in cooperation with the Republic of Chile. The Joint ALMA Observatory is operated by ESO, AUI/NRAO and NAOJ. We acknowledge grants from the Ministry of Science and Technology of Taiwan (MoST 104-2119-M-001-015-MY3 and 107-2119-M-001-040-MY3) and the Academia Sinica (Investigator Award AS-IA-108-M01).

REFERENCES

Balick, B., & Frank, A. 2002, ARA&A, 40, 439

Balick, B., Frank, A., & Liu, B. 2019, ApJ, 877, 30

Balick, B., Gomez, T., Vinković, D., et al. 2012, ApJ, 745, 188

Balick, B., Huarte-Espinosa, M., Frank, A., et al. 2013, ApJ, 772, 20

Bujarrabal, V., Castro-Carrizo, A., Alcolea, J., & Sánchez Contreras, C. 2001, A&A, 377, 868

Bujarrabal, V., Castro-Carrizo, A., Alcolea, J., et al. 2016, A&A, 593, A92

Bujarrabal, V., Castro-Carrizo, A., Van Winckel, H., et al. 2018, A&A, 614, A58

Cox, P., Huggins, P. J., Maillard, J.-P. et al. 2003, ApJ, 586, L87

Cox, P., Lucas, R., Huggins, P. J., et al. 2000, A&A, 353, L25

Davis, C. J., Smith, D. M., Gledhill, T. M., & Varricatt, W. P. 2005, MNRAS, 360, 104

Dharmawardena, T. E., Kemper, F., Scicluna, P., et al. 2018, MNRAS, 479, 536

de Vries, B. L., Maaskant, K. M., Min, M. et al. 2015, A&A, 576, A98

Górny, S. K., Tylenda, R., & Szczerba, R. 1994, A&A, 284, 949

Hsu, M.-C., & Lee, C.-F. 2011, ApJ, 736, 30

Hu, J. Y., Slijkhuis, S., Nguyen-Q-Rieu, & de Jong, T. 1993, A&A, 273, 185

Huang, P.-S., Lee, C.-F., Moraghan, A., & Smith, M. 2016, ApJ, 820, 134

Huggins, P. J. 2007, ApJ, 663, 342

Justtanont, K., Skinner, C. J., Tielens, A. G. G. M., Meixner, M., & Baas, F. 1996, ApJ, 456, 337

Kwok, S., Su, K. Y. L., & Hrivnak, B. J. 1998, ApJL, 501, B117

Lee, C.-F., & Sahai, R. 2003, ApJ, 586, 319

Lee, C.-F., Sahai, R., Sánchez Contreras, C. et al. 2013a, ApJ, 777, 37

Lee, C.-F., Stone, J. M., Ostriker, E. C., & Mundy, L. G. 2001, ApJ, 557, 429

Lee, C.-F., Yang, C.-H., Sahai, R., & Sánchez Contreras, C. 2013b, ApJ, 770, 153

Matt, S., Frank, A., & Blackman, E. G. 2006, ApJL, 647, L45

Meixner, M., Ueta, T., Bobrowsky, M., & Speck, A. 2002, ApJ, 571, 936

Montgomery, M. M. 2012, ApJ, 745, B25

Riera, A., Velázquez, P. F., Raga, A. C., Estalella, R., & Castrillón, A. 2014, A&A, 561, A145

Sahai, R. 2004, in ASP Conf. Proc. 313, Asymmetrical Planetary Nebulae III: Winds, Structure and the Thunderbird, ed. M. Meixner, J. H. Kastner, B. Balick, & N. Soker (San Francisco, CA: ASP), 141

Sahai, R., Bujarrabal, V., Castro-Carrizo, A., Zijlstra, A. 2000, A&A, 360, L9

Sahai, R., Hines, D. C., Kastner, J. H., et al. 1998, ApJL, 492, L163

Sahai, R., Morris, M., Sánchez Contreras, C., & Claussen, M. 2007, 134, 2200

Sahai, R., Scibelli, S., & Morris, M. R. 2016, ApJ, 827, 92

Sahai, R., & Trauger, J. T. 1998, AJ, 116, 1357

Sánchez Contreras, C., Alcolea, J., Bujarrabal, V., Castro-Carrizo, A., et al. 2018, A&A, 618, A164

Soker, N., & Mcley, L. 2013, ApJL, 772, B22

Terquem, C. 1998, ApJ, 509, 819

Velázquez, P. F., Raga, A. C., Riera, A., et al. 2012, MNRAS, 419, 3529

Velázquez, P. F., Raga, A. C., Cantó, J., Schneiter, E. M., & Riera, A. 2013, MNRAS, 428, 1587

Velázquez, P. F., Riera, A., Raga, A. C., & Toledo-Roy, J. C. 2014, 794, 128

Wiescher, M., Görres, J., Uberseder, E., Imbriani, G., & Pignatari, M. 2010, ARNPS, 60, 381

Woods, P. M., Nyman, L.-Å., Schöier, F. L., et al. 2005, A&A, 429, 977

Zuckerman, B., & Dyck, H. M. 1986, ApJ, 311, 345

This 2-column preprint was prepared with the AAS LaTeX macros v5.2.

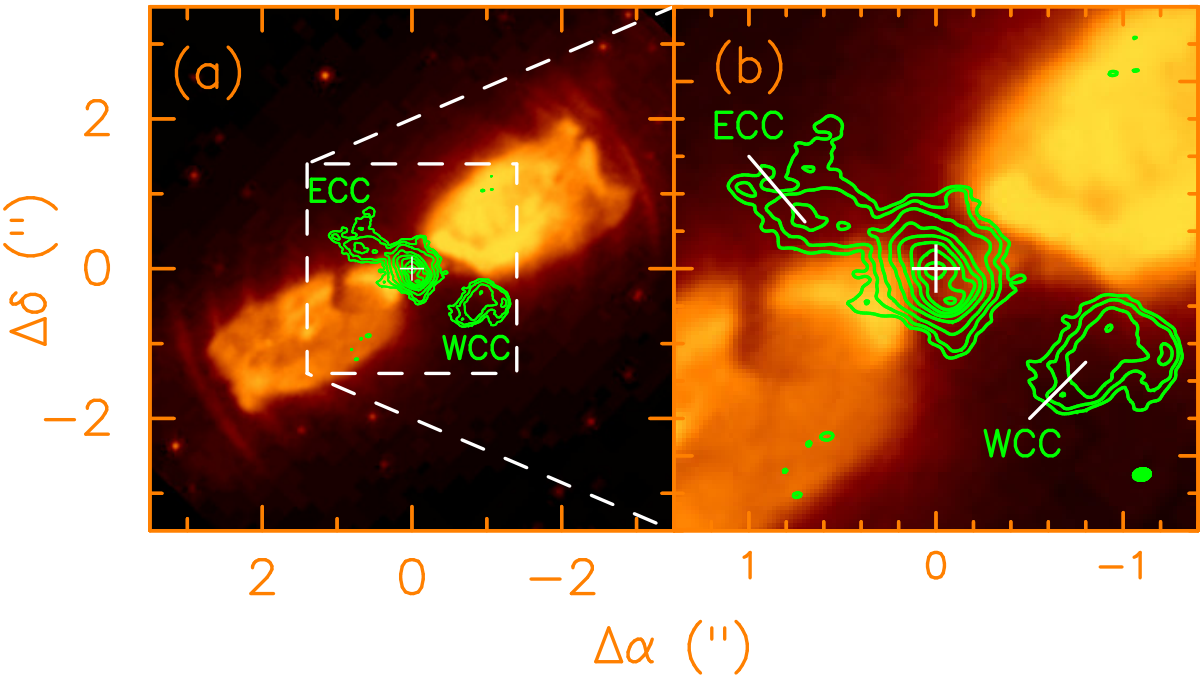

Fig. 1.— (a) The 350 GHz continuum map (green contours) of I17150 observed by the ALMA, superimposed on the *HST* image obtained with filter F606W (Kwok et al. 1998). In continuum, three components, with one at the center, one in the east, and one in the west, are detected in the waist of the optical bipolar lobe. (b) A zoom-in to the inner region. The cross marks the primary peak of the central component. The beam in the bottom-right corner has a size of $\sim 0\farcs9 \times 0\farcs06$ with a major axis at P.A. $\sim -81°$. The contour levels are 3σ, 6σ, and 12σ for the first three contours and have a step of 12σ for the other contours, where $\sigma \simeq 0.1$ mJy beam^{-1}.

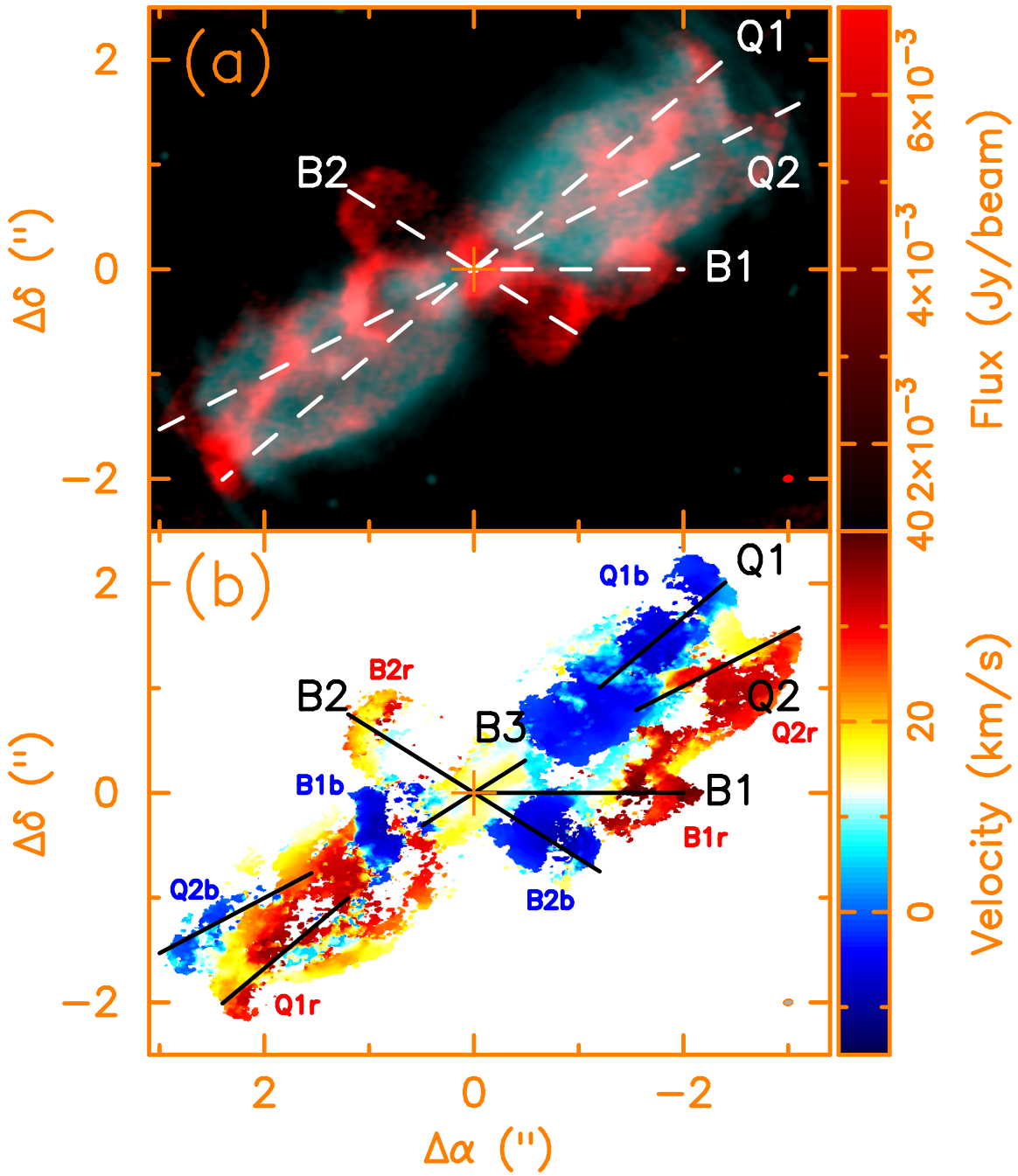

Fig. 2.— (a) Total intensity map (red image) plotted on top of the *HST* image (turquoise image) and (b) intensity-weighted velocity map of I17150 in CO $J = 3$–2 line. The dashed lines and solid lines indicate the outflow axes. Blueshifted and redshifted outflow lobes are labeled with symbols b and r, respectively. The low-velocity emission at the center (yellow color) is from outflow B3 as indicated by the outflow axis. The beam size is $\sim 0\farcs09 \times 0\farcs06$ with a major axis at P.A. $\sim -81°$.

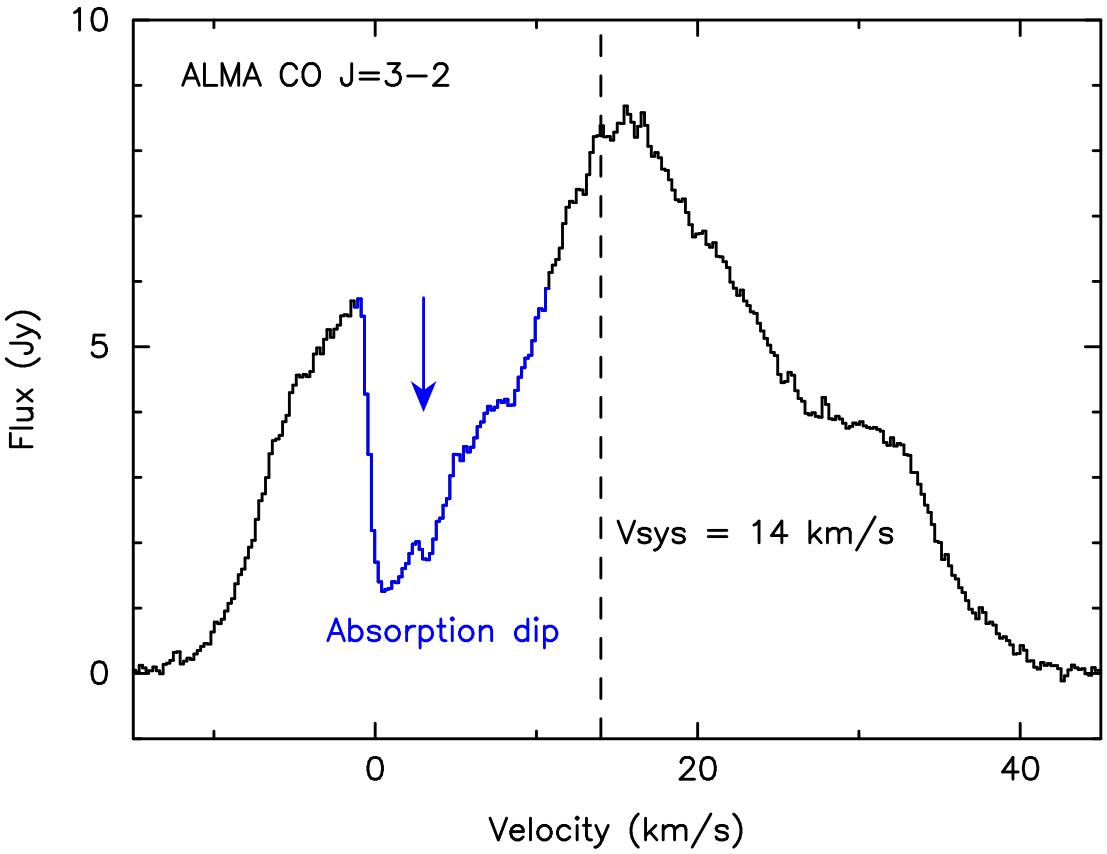

Fig. 3.— The CO $J = 3$–2 line profile of I17150, averaged over an elliptical region with a major axis of $7''$, a minor axis of $4''$, and P.A. $= -56°$, covering all the outflows. Blue curve marks the absorption dip at the velocity from -1 to 12 km s^{-1}.

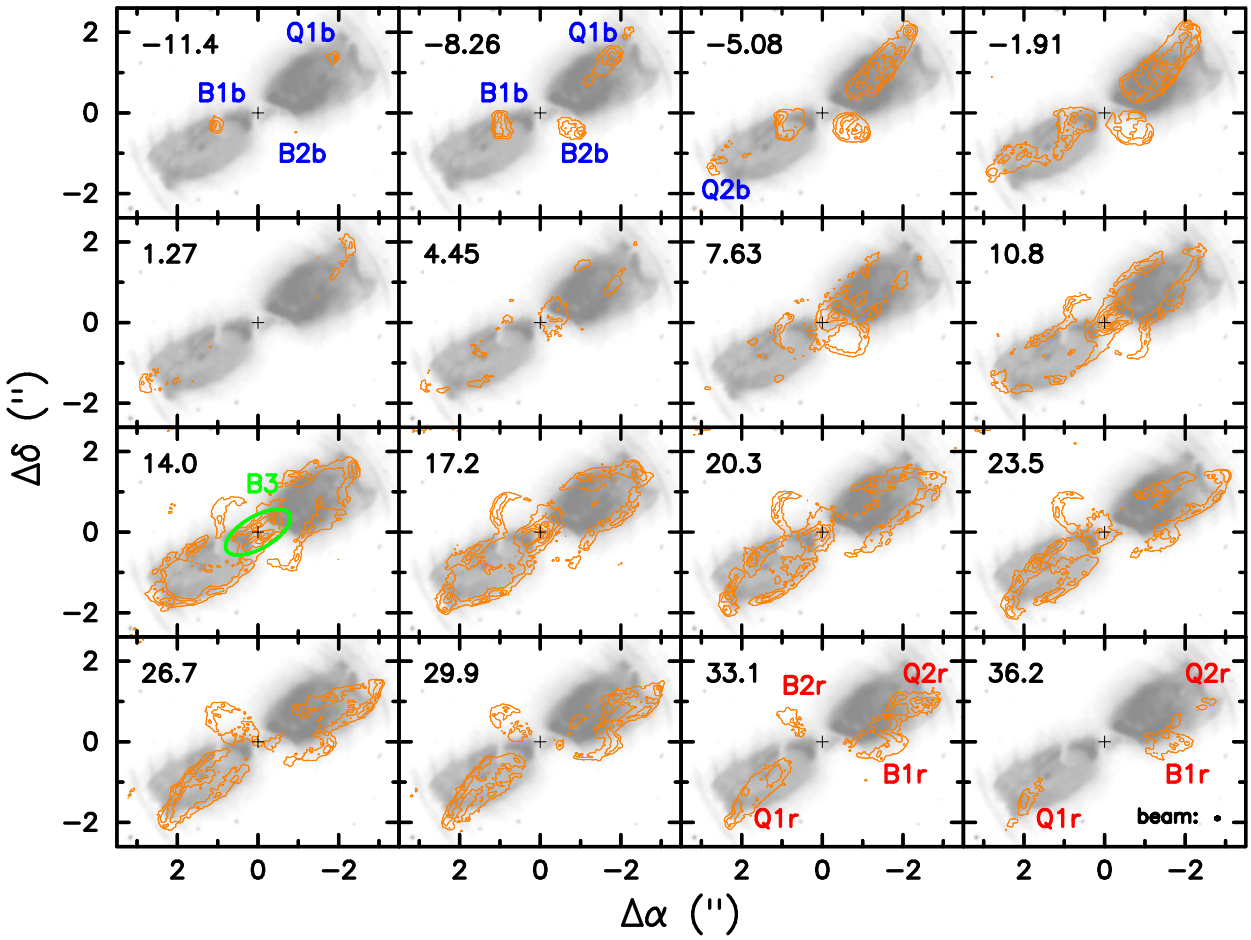

Fig. 4.— The CO $J = 3$–2 channel maps of I17150. The velocity in each channel is indicated at the upper-left corner. The systemic velocity is ~ 14 km s^{-1}. The beam size is $\sim 0\farcs09 \times 0\farcs06$ with a major axis at P.A. $\sim -81°$. The contours start from 3σ with a step of 3σ, where $\sigma \simeq 3$ mJy beam^{-1}. The quadrupolar outflow lobes are labeled with Q1b, Q1r, Q2b, and Q2r. The bipolar outflow lobes are labeled with B1b, B1r, B2b, and B2r. The outflow at the base of the outflows is labeled with B3.

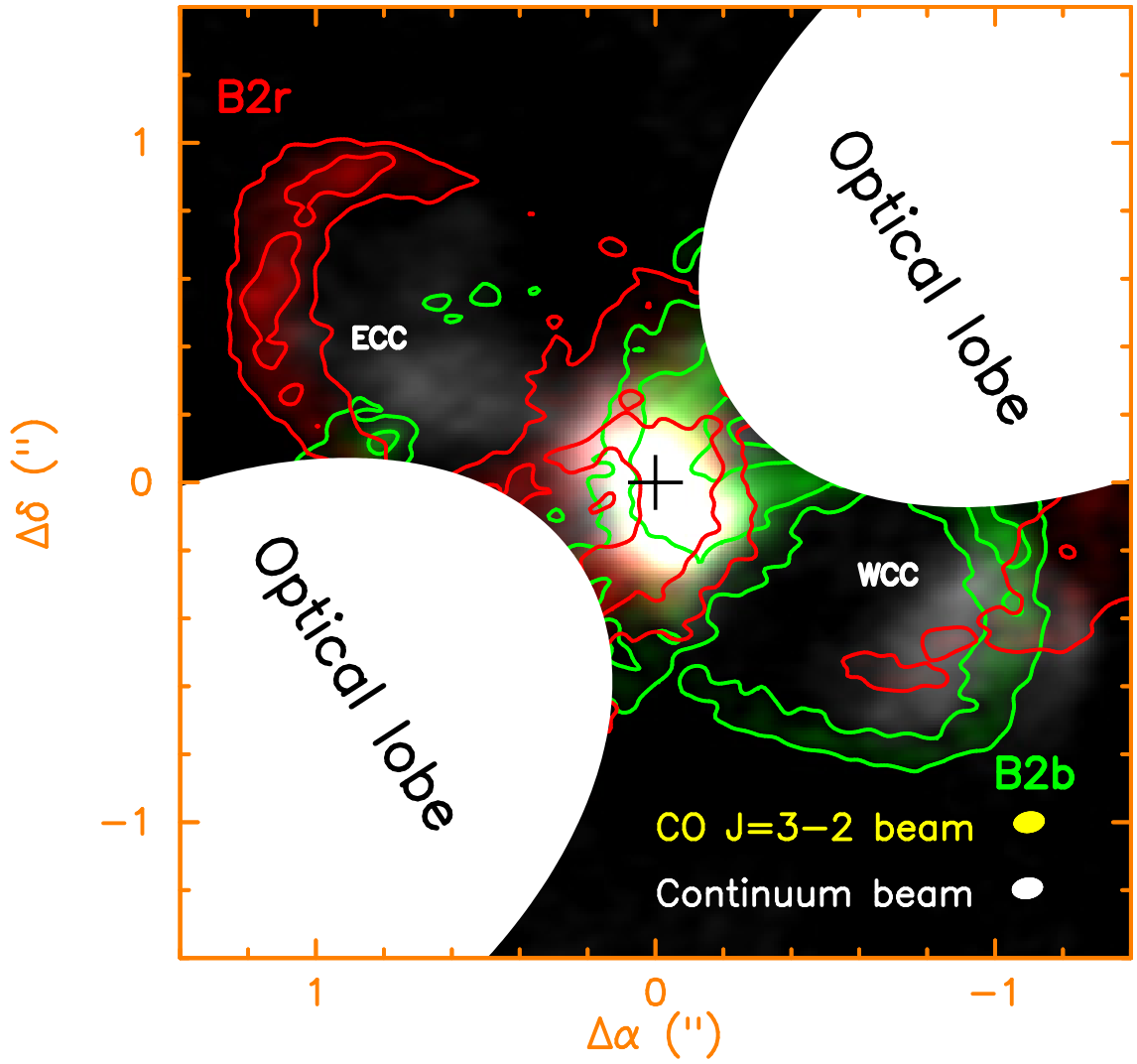

Fig. 5.— The morphological connection between the continuum and outflows in the inner region of I17150. It shows the blueshifted (at 7.63 km s^{-1}, green image and contours) and redshifted (at 20.3 km s^{-1}, red image and contours) CO channel maps of the outflows, superimposed on the continuum map (grey-scale image). The outflow B2 is roughly aligned with the axis connecting the eastern and western continuum components. The contour levels of the CO emissions are the same as those in Figures 4.

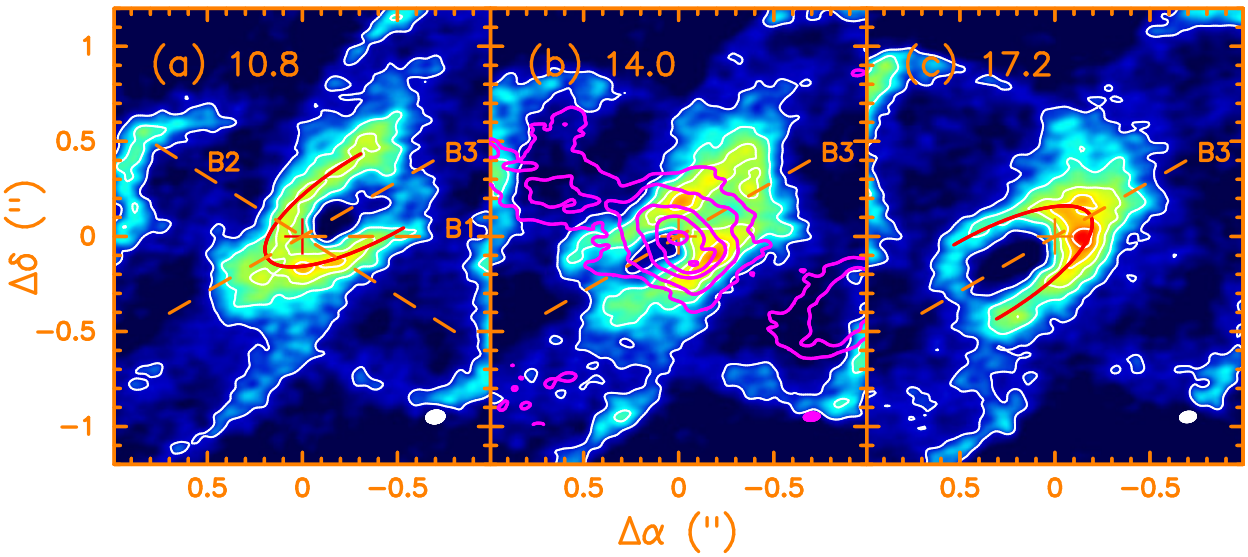

Fig. 6.— The low-velocity CO channel maps of outflow B3 in I17150. The velocity in each channel is indicated in the upper-left corner. Panels (a) and (c) show the low-velocity blueshifted and redshifted shells, respectively, as indicated by the red curves (which are the fits using a half ellipse). Panel (b) shows the continuum map (magenta contours) superimposed on the CO map of the outflow at the systemic velocity of 14 km s^{-1}, in order to reveal their morphological connection. The beam and contour levels of the CO maps are the same as those in Figure 4.

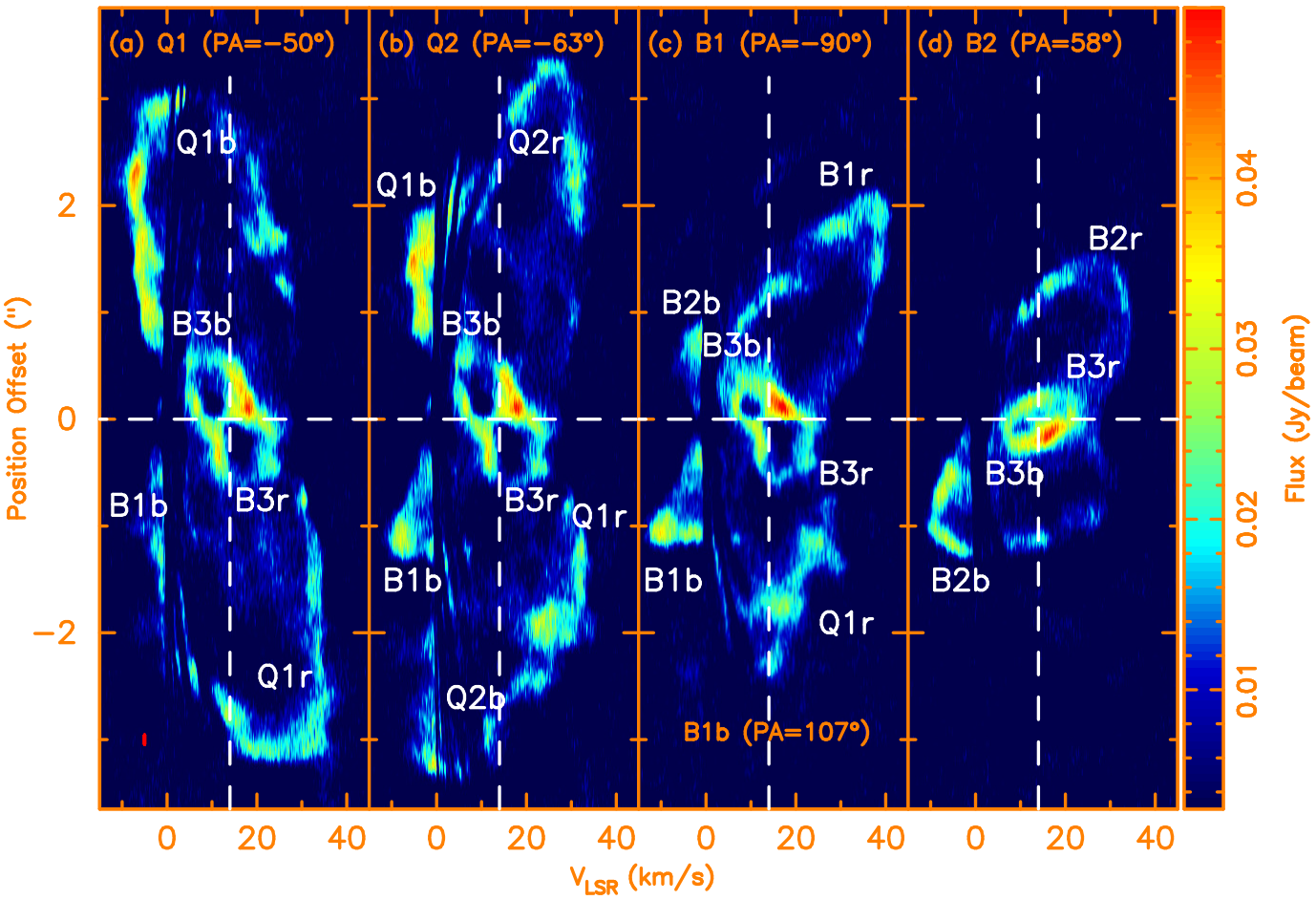

Fig. 7.— PV diagrams of CO $J = 3$–2 emissions cut along the axes of outflows (a) Q1, (b) Q2, (c) B1 (B1r and B1b), and (d) B2. Vertical dashed lines indicate the systemic velocity of 14 km s^{-1} and horizontal dashed lines indicate the central source position. The red bar at the bottom-left corner indicates the resolution for the PV diagram.

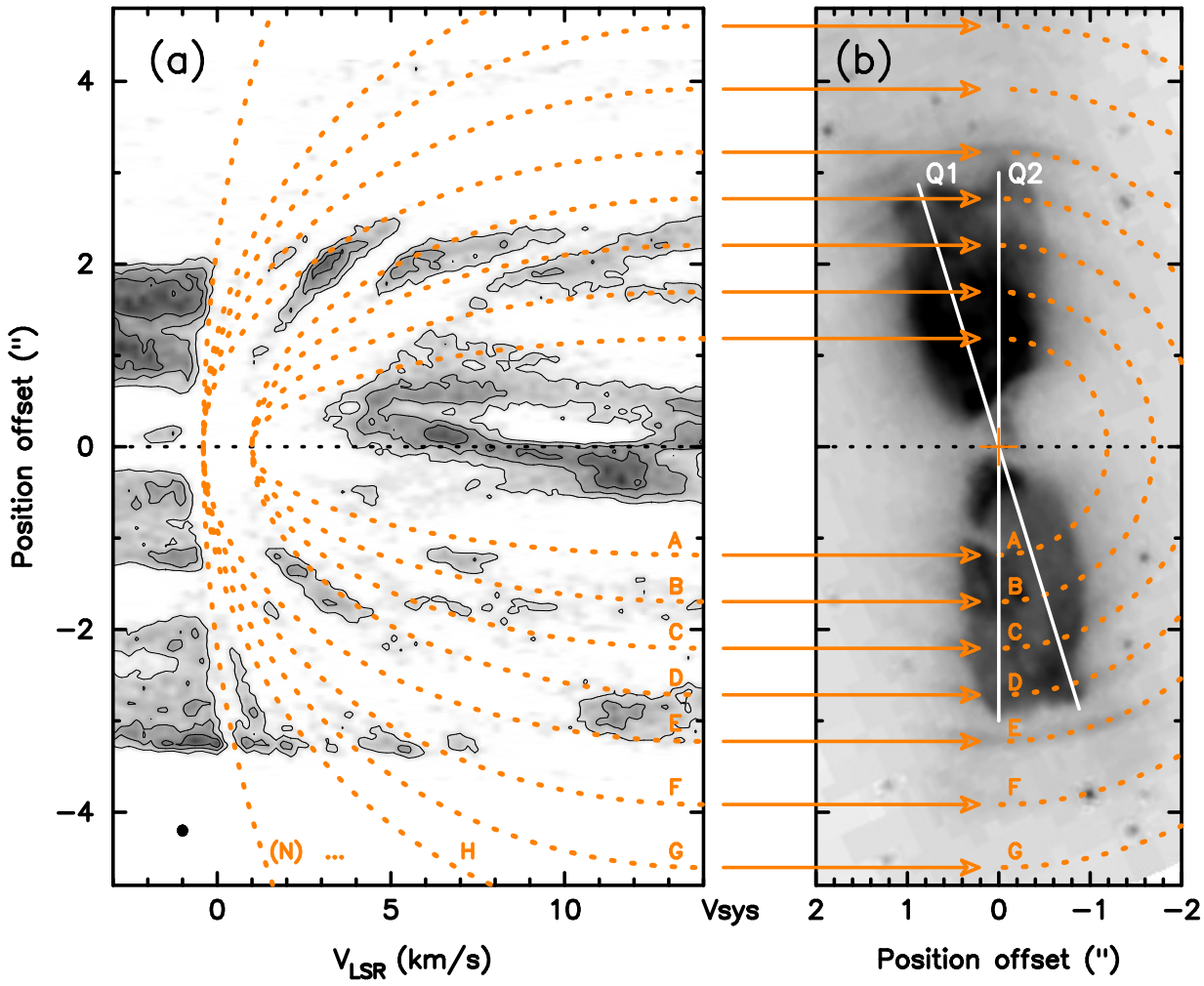

Fig. 8.— The connection of the CO PV diagram with the optical arcs. (a) shows the PV diagram of CO cut along the axis of outflow Q2, as extracted from the blueshifted part of Figure 7b. The contours start from 3σ with a step of 3σ, where $\sigma \simeq 3$ mJy beam^{-1}. The dashed lines show the absorption curves. These curves can be linked to the optical arcs seen in the *HST* image (Kwok et al. 1998) shown in panel (b).

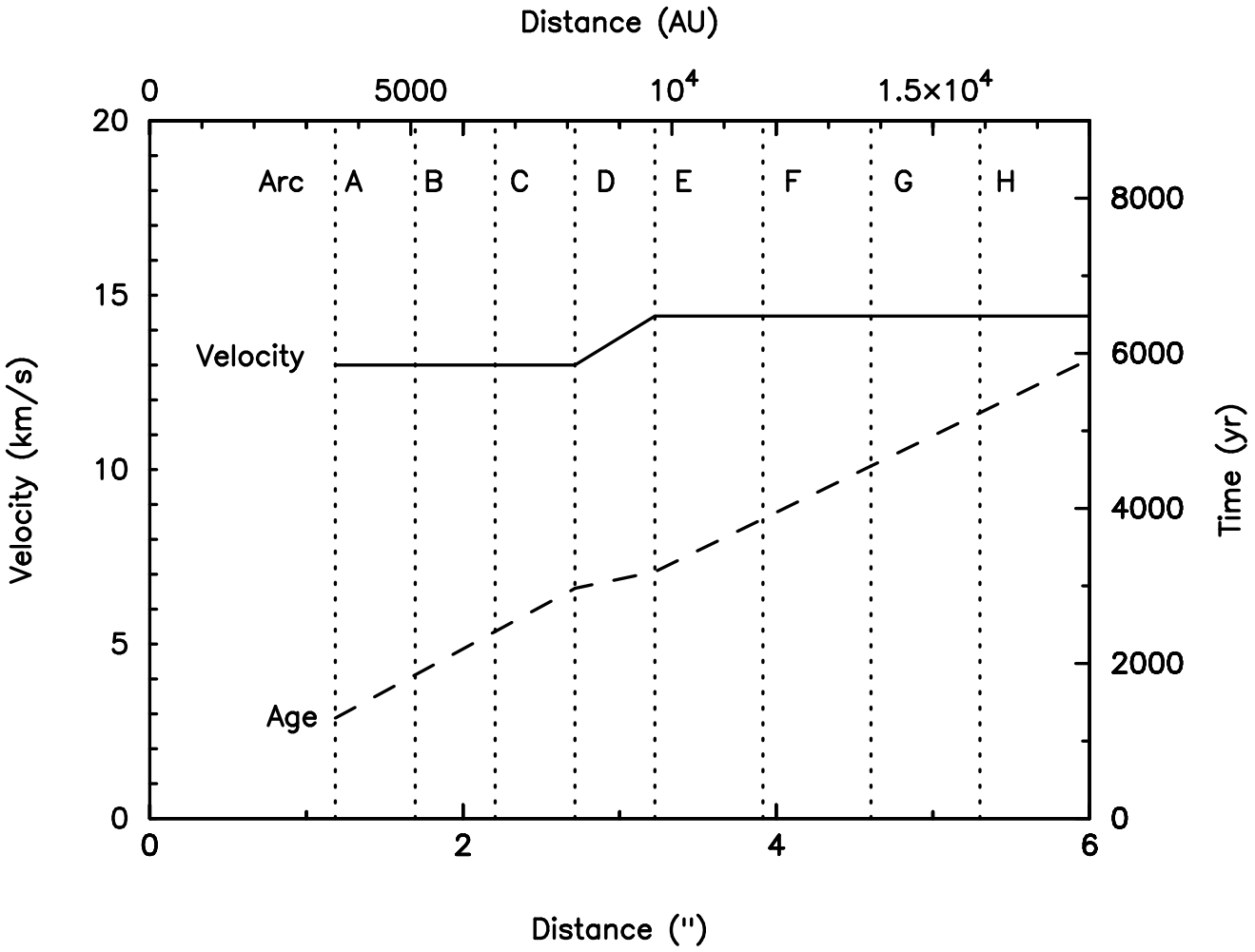

Fig. 9.— The expansion velocity and the dynamical age of the arcs obtained from our model (see text). The expansion velocity decreases slightly from 14.4 to 13 km s^{-1} from arc E to arc D.

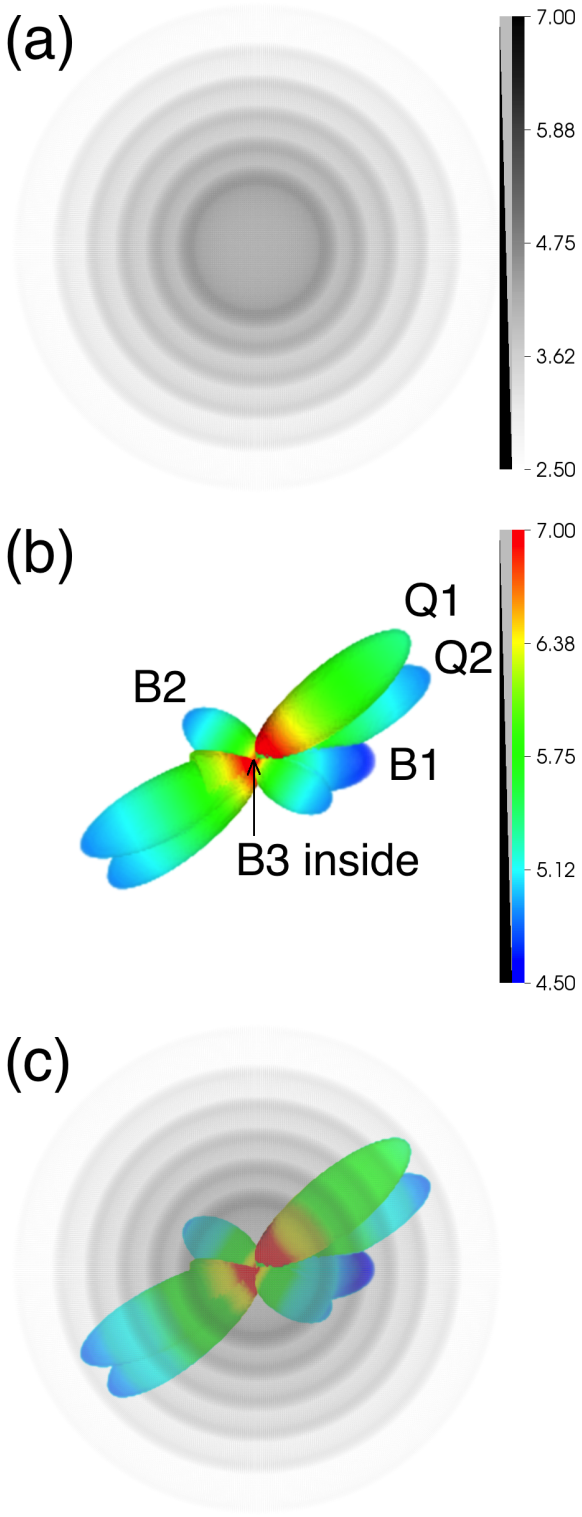

Fig. 10.— Our AGB wind and outflow model for I17150. (a) shows the AGB wind. The semi-transparent grey color represents the number density of H_2 in log scale. (b) shows the outflows. The colors represent the number density of H_2 in log scale. (c) shows the combination of the two.

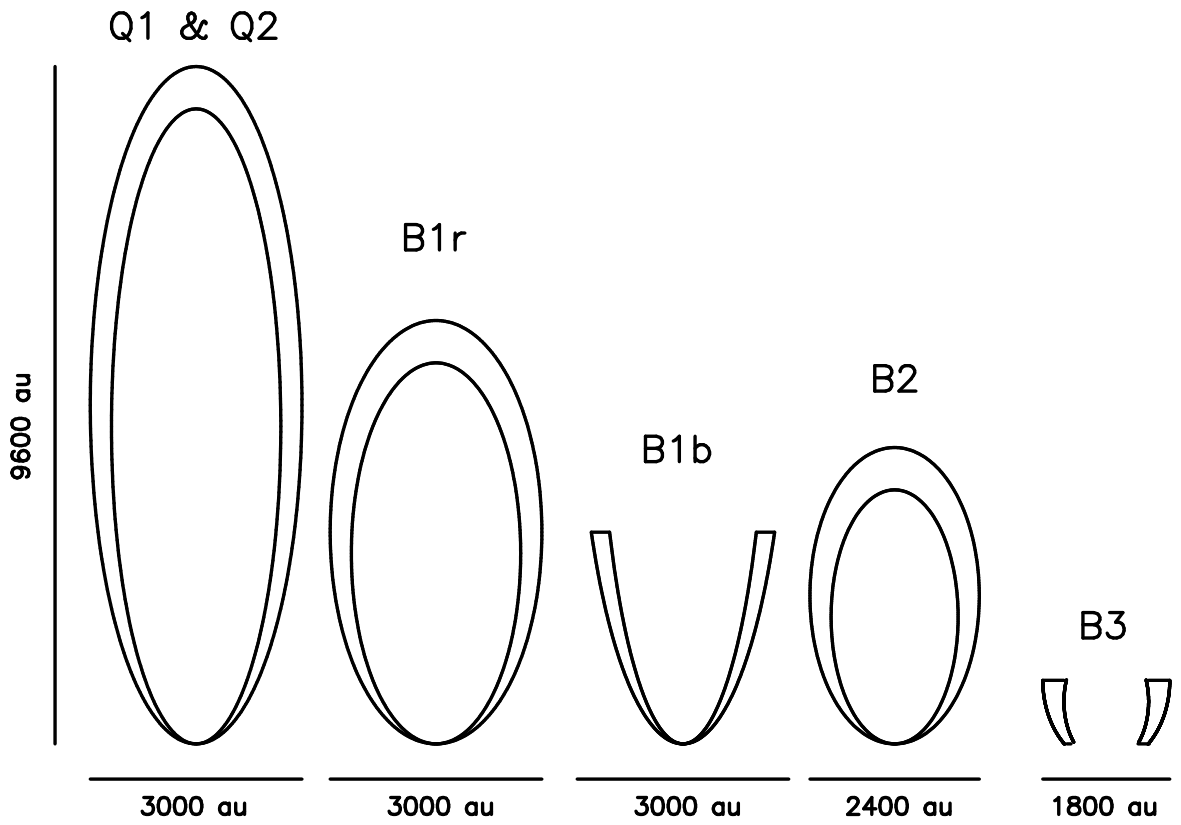

Fig. 11.— The outflow lobes in our model with their lengths and widths indicated. Each lobe is bounded by two ellipsoids/half-ellipsoids (see text).

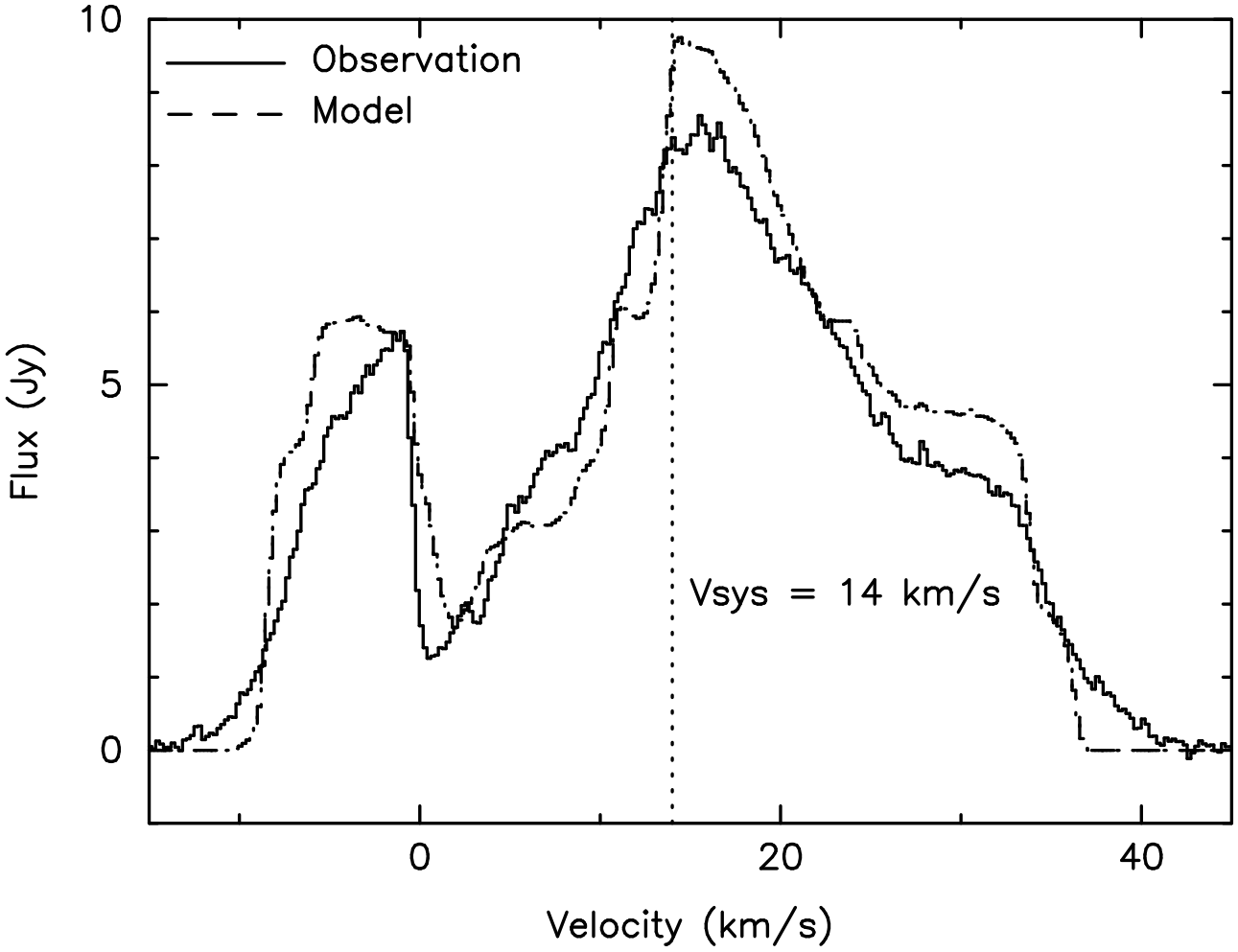

Fig. 12.— Comparison of the CO $J = 3$–2 line profile in I17150 between our model (dashed line) and the observation (solid line).

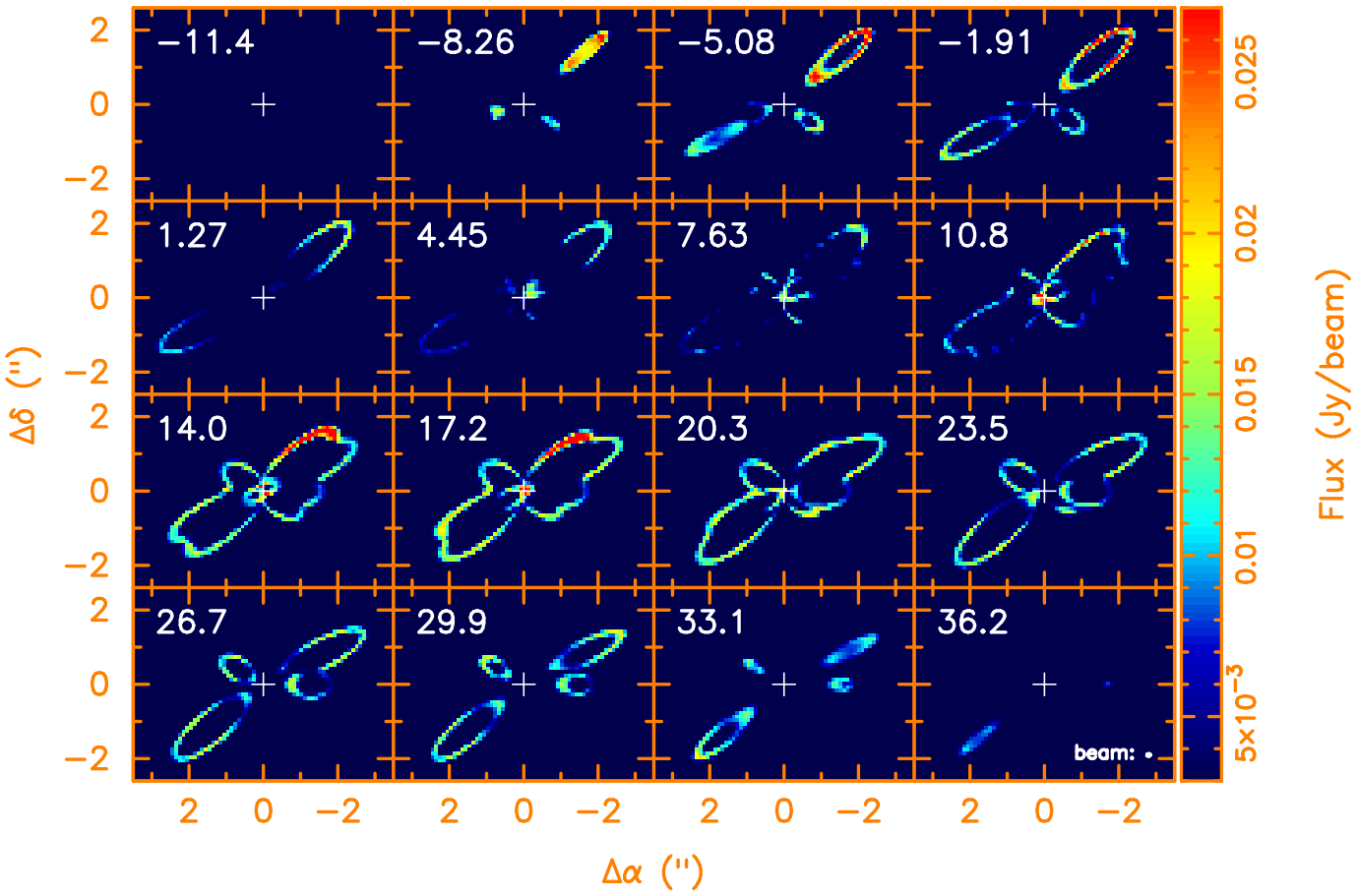

Fig. 13.— Simulated CO $J = 3$–2 channel maps to be compared with the observations. The beam is the same as that in Figure 4.

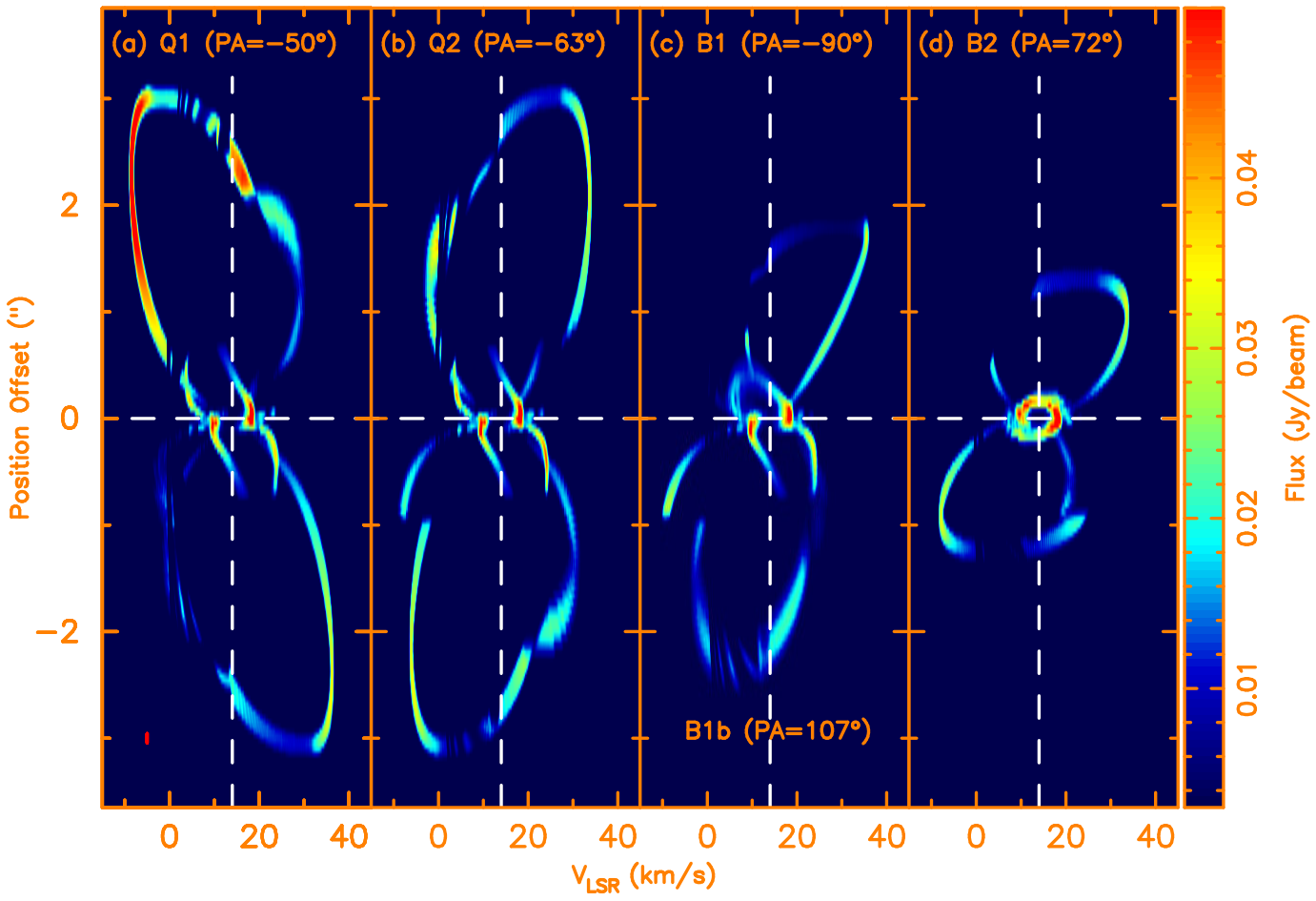

Fig. 14.— Simulated PV diagrams of CO $J = 3$–2 emissions cut along the axes of outflows Q1, Q2, B1 (B1r and B1b), and B2.

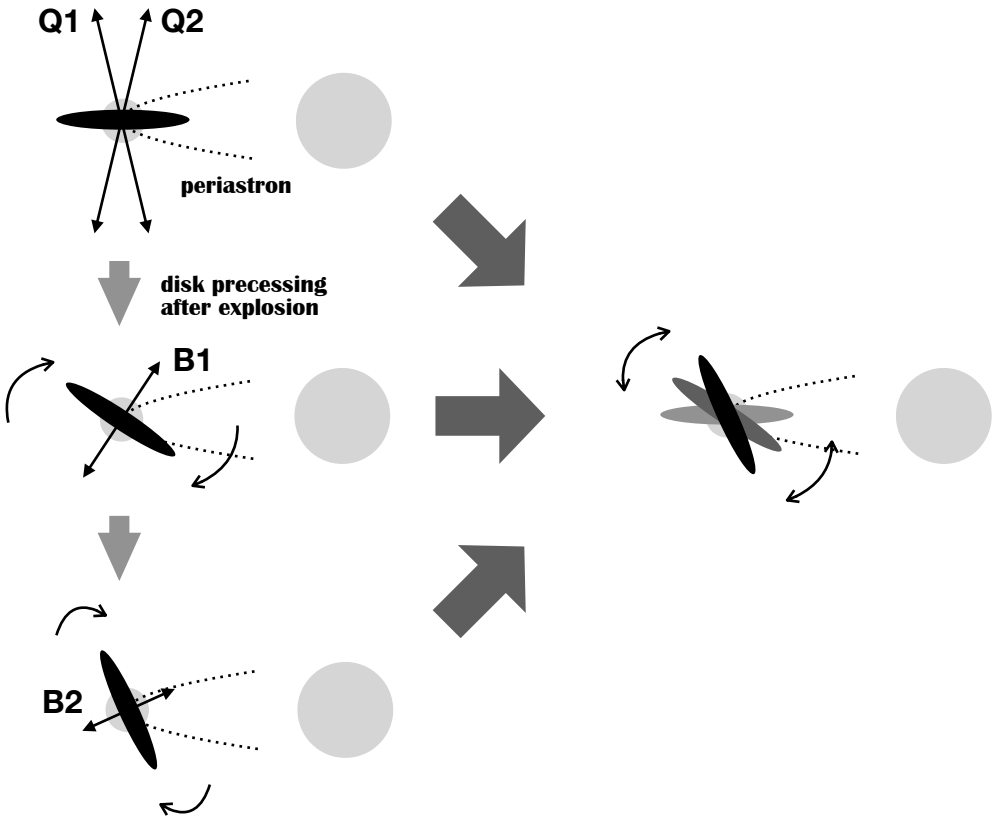

Fig. 15.— Schematic diagram of the ejection period. At the first stage, the disk plane was on the orbital plane before the quadrupolar outflow was produced by an explosive event when the companion passed the periastron. At the second stage, the disk started to precess due to the explosion and the outflow axis was changing with time. When the companion passed through the periastron again, it produced outflow B1. The third stage was similar to the second stage, except the larger inclination angle from the oribtal plane, and the outflow B2 was produced when the companion passed through the periastron.

Table 1: Best-fit Values of Model Parameters for the AGB Wind

Radius	
$r_{\rm A}$	3555 au
$r_{\rm B}$	5085 au
$r_{\rm C}$	6615 au
$r_{\rm D}$	8145 au
$r_{\rm E}$	9675 au
$r_{\rm F}$	11745 au
$r_{\rm G}$	13815 au
$r_{\rm H}$	15885 au
Temperature	
$T_{\rm a,0}$	10 K
$\gamma_{\rm A}$	-1

Table 2: Best-fit Values of Model Parameters for the Outflows

Outflow lobe	l_f (au)	D_f (au)	i (°)	P.A. (°)	v_f (km s^{-1})	θ_f (°)	β_f	$n_{f,0}$ (cm^{-3})	$T_{f,0}$ (K)	γ_f
Q1b, Q1r	9600	3000	−8, 8	−50, 130	130	17	1	2.3×10^5, 7.5×10^4	150, 80	0.8
Q2b, Q2r	9600	3000	−6, 6	117, −63	130	17	1	7.5×10^4	80	0.8
B1b, B1r	3000, 6000	3000	−12, 12	107, −90	100	17	1	3.8×10^4	150, 100	0.8
B2b, B2r	4200	2400	−8, 8	−122, 58	100	26	1	7.5×10^4	80	0.8
B3b, B3r	900	1800	−6, 6	−60, 120	80[a]	45	–	3.8×10^4	133	-0.5

a: $v_{\rm B3z,0} = 80$ km s^{-1}, $v_{\rm B3R,0} = 9$ km s^{-1}, and $v_{\rm B3R,1} = 3$ km s^{-1}